Multifrequency subsurface sensing in the presence of a moderately rough air–soil interface via quasi-ray Gaussian beams

Vincenzo Galdi,[1] Haihua Feng, David A. Castañon, and W. Clem Karl

Department of Electrical and Computer Engineering, Boston University, Boston, Massachusetts, USA

Leopold B. Felsen[2]

Department of Aerospace and Mechanical Engineering and Department of Electrical and Computer Engineering, Boston University, Boston, Massachusetts, USA

Received 12 November 2001; revised 23 February 2002; accepted 1 April 2002; published 7 December 2002.

[1] An adaptive framework is presented for frequency-stepped ground-penetrating radar (GPR) imaging of low-contrast buried objects in the presence of a moderately rough air–soil interface, with potential applications intended in the area of humanitarian demining. The proposed approach, so far restricted to two-dimensional (2-D) geometries, works with sparse data and relies on recently developed problem-matched narrow-waisted Gaussian beam (GB) algorithms as fast forward scattering predictive models to estimate and compensate for the effects of the coarse-scale roughness profile. Possible targets are subsequently imaged by inverting the Born-linearized subsurface scattering model via object-based curve evolution (CE) techniques. This frequency domain (FD) strategy implements a further step in our planned sequential approach toward a physics based, robust, and numerically efficient framework for rough surface underground imaging in both FD and time domain (TD). Numerical experiments indicate that the proposed framework is attractive from both computational and robustness viewpoints. The results in this paper could also be used for synthesis of TD illumination (in a previous study [*Galdi et al.*, 2001b], we have dealt with wideband illumination directly in the TD). *INDEX TERMS:* 0629 Electromagnetics: Inverse scattering; 0659 Electromagnetics: Random media and rough surfaces; 0669 Electromagnetics: Scattering and diffraction; *KEYWORDS:* ground penetrating radar, rough surfaces, Gaussian beams

Citation: Galdi, V., H. Feng, D. A. Castañon, W. C. Karl, and L. B. Felsen, Multifrequency subsurface sensing in the presence of a moderately rough air–soil interface via quasi-ray Gaussian beams, *Radio Sci.*, *37*, 8007, doi:10.1029/2001RS002557, 2002. [printed *38*(2), 2003]

1. Introduction

[2] In many ground-penetrating radar (GPR) applications, such as antipersonnel land mine remediation, one is typically interested in detecting, localizing and characterizing shallowly buried small targets with constitutive properties very close to those of the background soil [*Dubey et al.*, 2001]. In such applications, a major source of corruption and distortion in the interrogating signals is related to reflection from, and (double) transmission through, the irregular unknown air–soil interface. Traditional approaches to cope with this problem tend to model the roughness effect through a purely statistical Monte Carlo-based approach, e.g., via additive colored Gaussian noise [*Dogaru and Carin*, 1998; *Yang and Rappaport*, 2001]. Such techniques perform reasonably well in detection problems in the presence of small roughness [*Dogaru et al.*, 2001; *Zhan et al.*, 2001], but have been found to yield limited accuracy and reliability concerning localization and classification for moderate roughness [*Feng et al.*, 2000b].

[3] In an ongoing series of recent investigations, so far restricted to 2-D geometries, we have been working

[1] On leave from University of Sannio, Benevento, Italy.

[2] Also at Polytechnic University (Emeritus), Brooklyn, New York, USA.

0048-6604/02/2001RS002557$11.00

toward a more robust *adaptive* approach for imaging low-contrast mine-like targets shallowly buried under a moderately rough air–soil interface, using both frequency-stepped and pulsed GPRs. Our approach is based on prior estimation of the coarse-scale roughness profile. In this connection, a low-dimensional parameterization of the unknown interface is used in conjunction with physics-based approximate forward scattering models based on *narrow-waisted* quasi-ray Gaussian beams (GB) [*Galdi et al.*, 2001a, 2002b], and the interface estimation problem is posed as a nonlinear optimization problem [*Galdi et al.*, 2002a, 2003]. The estimated roughness profile is then used to compensate for the effect of the air–soil interface in the received data. The corrected data are used subsequently to image the subsurface region and localize possible anomalies. At this stage, statistical models may be useful to account for noise, measurement uncertainty, and residual unmodeled effects.

[4] In our investigation, we have proceeded along two parallel routes, in the frequency domain (FD) and time domain (TD), in order to explore both frequency-stepped and direct TD pulsed operation for eventual time-resolved GPR scenarios. In particular, the present paper (together with the work of *Galdi et al.* [2002a]) deals with the frequency-stepped FD formulation, in contrast with the direct TD formulation of *Galdi et al.* [2001b, 2003]. Both the FD and TD formulations have most of the technical background related to the GB forward solvers in common. The data processing, however, is significantly different. Although the FD approach in the present paper and in the work of *Galdi et al.* [2002a] could be applied, via Fourier inversion, also to *wideband* TD data, *Galdi et al.* [2001b, 2003] have pursued the above alternative *direct* TD processing route, which they believe to be better matched to the wideband *physics* of the problem, with better insight as a consequence.

[5] Referring to the works of *Galdi et al.* [2001a, 2001b, 2002b] for technical background on the GB forward scattering algorithms, our focus in this paper is on the description and evaluation of the *FD inversion* scheme, in particular on its performance in connection with *object-based* reconstruction. While the inverse scattering algorithms utilized here are *formally* independent of the chosen forward solver, the *overall performance* depends *strongly* on this choice, which in our case is based on GBs [for details, see *Galdi et al.*, 2001a, 2001b, 2002b].

[6] The rest of this paper is organized as follows. In section 2, the problem is formulated and the underlying geometry is described. In section 3, the multifrequency rough surface estimation algorithm of *Galdi et al.* [2002a] is briefly reviewed. Section 4 deals with the subsurface imaging problem in the presence of a known air–soil moderately rough interface. Numerical results, limitations of the approach, and computational issues are discussed in section 5. Brief conclusions are given in section 6.

2. Problem Statement

[7] We refer to the 2-D problem geometry sketched in Figure 1, where the soil is modeled as a homogeneous lossy dielectric half-space with known relative permittivity ϵ_{r1} and weak conductivity σ_1, bounded by a moderately rough interface with profile $z = h(x)$. A shallowly buried dielectric mine-like target, with negligible conductivity $\sigma_2 \approx 0$ and relative permittivity ϵ_{r2} close to that of the background soil ($|\epsilon_{r2} - \epsilon_{r1}|/\epsilon_{r1} \ll 1$), is assumed to occupy the region $\mathcal{D}$ in the half-space $z < h(x)$. Illumination is furnished by a transverse magnetic (TM)-polarized electromagnetic (EM) field with y-directed electric field and suppressed time dependence $\exp(-i\omega t)$. The actual interrogating field distribution is specified on a (projected) large truncated aperture of width d at $z = z_A$, and is assumed to be sufficiently well collimated to permit approximation of the y-directed incident electric field E^i by a truncated tapered plane wave

$$E^i(\mathbf{r}, \omega) \sim g(x_B)\exp(ik_0 z_B). \tag{1}$$

Here $\mathbf{r} \equiv (x, z)$, and $k_0 = \omega\sqrt{\epsilon_0\mu_0} = 2\pi/\lambda_0$ is the free-space wave number, with ϵ_0, μ_0 denoting the free-space permittivity and permeability, respectively, and λ_0 denoting the free-space wavelength. Bold face symbols denote vector quantities. Moreover, $g(x_B)$ is a spatial taper, and (x_B, z_B) are beam-centered coordinates,

$$\begin{bmatrix} x_B \\ z_B \end{bmatrix} = \begin{bmatrix} \cos\theta_A & \sin\theta_A \\ \sin\theta_A & -\cos\theta_A \end{bmatrix} \begin{bmatrix} x - x_A \\ z - z_A \end{bmatrix}, \tag{2}$$

with θ_A and x_A denoting the tilt angle of the impinging illumination relative to the *z axis* and the spatial displacement of its maximum, respectively, chosen so that the illumination tapers to zero and vanishes for $|x| > d/2$ (Figure 1). In what follows, the soil is assumed to be slightly lossy, i.e., $\sigma_1/(\omega\epsilon_{r1}\epsilon_0) \ll 1$, and attention is restricted to the y-directed electric field $E(\mathbf{r}, \omega)$ from which all other field quantities of interest can be computed via Maxwell's equations.

[8] The final goal of this investigation is the estimation, from sparse multifrequency scattered field observations, of the constitutive properties (dielectric permittivity) of the target as well as its geometrical features (position and shape). To this end, the y-directed backscattered electric field at N_ω operating angular frequencies $\omega_1, \ldots, \omega_{N_\omega}$ is sampled at N_r fixed receiver locations $x_1^r, \ldots, x_{Nr}^r$ on the plane $z = z^r$ (Figure 1). In our numerical experiments in section 5, this set of $N_r \times N_\omega$ complex (magnitude and phase) samples, which constitutes the observation term of the inverse problem, will be generated synthetically via a rigorous full-wave

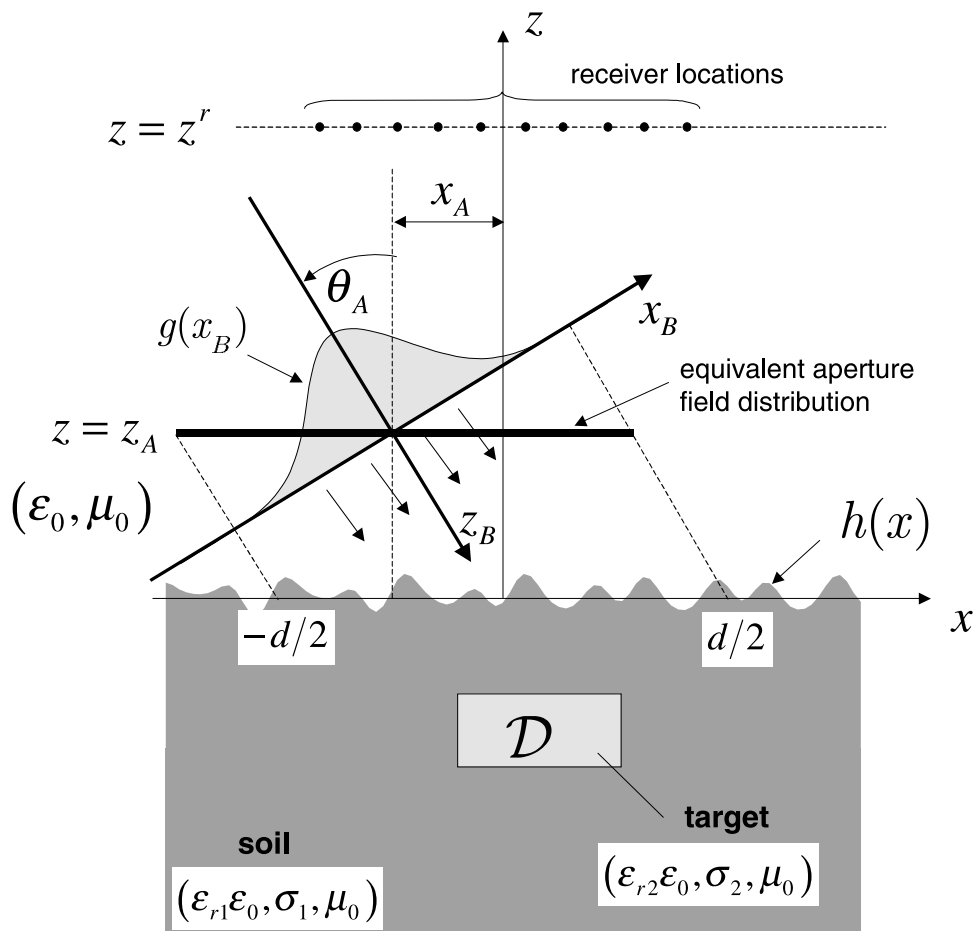

Figure 1. Problem geometry. An aperture-generated, quasi-plane wave, TM-polarized time-harmonic field impinges from free space onto a dielectric half-space with known relative permittivity ϵ_{r1} and conductivity σ_1, bounded by a moderately rough interface profile $z = h(x)$, wherein a target with dielectric permittivity ϵ_{r2} and conductivity $\sigma_2 \approx 0$ occupies the region $\mathcal{D}$. The backscattered field at N_ω operating angular frequencies $\omega_1, \ldots, \omega_{N_\omega}$ is sampled at N_r fixed receiver locations $x_1^r, \ldots, x_{Nr}^r$ on the observation plane $z = z^r$.

solution of the forward scattering problem [*Leviatan and Boag*, 1987].

3. Rough Surface Profile Estimation

[9] The problem of estimating the coarse-scale profile of a moderately rough air–soil interface from multifrequency sparse backscattered field measurements, in the absence of buried targets, has been addressed by *Galdi et al.* [2002a]. The implementation strategy, based on the use of a low-order compact spline parameterization for the unknown profile $z = h(x)$ in conjunction with the Gabor-based narrow-waisted GB fast forward scattering model of *Galdi et al.* [2001a], is briefly reviewed here. As in the work of *Galdi et al.* [2002a], we assume that the coarse-scale interface profile can be approximated by a finite set of quartic B-spline basis functions $s_n^{(4)}(x)$ [*Shumaker*, 1981] with unknown coefficients h_n,

$$h(x) \approx \sum_{n=1}^{N} h_n s_n^{(4)}(x). \tag{3}$$

Given the set of backscattered field observation data $\mathcal{E}_{pq} \equiv \mathcal{E}(\mathbf{r}_p^r, \omega_q)$, at angular frequencies ω_q, $q = 1, \ldots, N_\omega$, and at receiver locations $\mathbf{r}_p^r = (x_p^r, z^r)$, $p = 1, \ldots, N_r$, and given a vector of spline coefficients $\underline{h} = \{h_n\}$, $n = 1, \ldots, N$, the surface estimation problem is posed as an optimization problem involving minimization of the cost functional

$$J_h(\underline{h}) = \sum_{p=1}^{N_r} \sum_{q=1}^{N_\omega} \nu_{pq} \left| \mathcal{E}_{pq} - E^r\left(\mathbf{r}_p^r, \omega_q; \underline{h}\right) \right|^2, \tag{4}$$

where $E^r(\mathbf{r}_p^r, \omega_q; \underline{h})$ represents the forward GB model prediction for the surface profile in (3) with specified surface coefficients $\underline{h}$ in the absence of the target, and $\nu_{pq} > 0$ are weight coefficients.

[10] As a fast forward scattering model, instead of the narrow-waisted paraxial beam-tracing scheme of *Galdi et al.* [2001a], we use here a slightly different GB algorithm based on Physical Optics (PO), detailed by *Galdi et al.* [2002b], which was found to be slightly more efficient. In this approach, the reflected field E^r in the absence of the target is assumed to be generated by a PO "equivalent current," which is parameterized in terms of x-domain discretized Gabor basis functions with narrow width $L \lesssim \lambda_0 \ll d$, centered on the Gabor lattice points $(x_m, h(x_m))$, $x_m = mL$. These initial conditions generate narrow-waisted quasi-ray GBs propagating along the local reflection directions, yielding the synthesis

$$E^r(\mathbf{r}, \omega) \sim \frac{1}{2} \sum_{|m| \leq (d/2L)} C_m^r(\omega) \tilde{B}_m^r(\mathbf{r}, \omega). \quad (5)$$

In (5), the Gabor coefficients C_m^r are estimated efficiently by sampling the PO "equivalent current" at the lattice points, whereas the GB propagators $\tilde{B}_m^r$ are approximated compactly via complex source point (CSP) paraxial asymptotics (see [*Galdi et al.*, 2002b, section III-B] for theoretical and computational details).

[11] To cope with the intrinsic nonlinearity of the cost functional in (4), i.e., with the possible presence of local minima, we use a global optimization strategy based on selective use of the various frequencies (frequency hopping) [*Chew and Lin*, 1995; *Belkebir and Tijhuis*, 1996]. This strategy, explored by *Galdi et al.* [2002a], was found to yield reasonably accurate and robust estimations. However, unlike in the work of *Galdi et al.* [2002a], here we account for the presence of the *underground target* when generating the synthetic observation data (see section 5.2.1).

4. Subsurface Imaging

[12] Once an estimate of the coarse-scale air–soil profile is available, the subsurface imaging problem can be addressed in a *quasi-deterministic* fashion. In this connection, we restrict consideration to the problem of subsurface sensing in the presence of a known roughness profile. Statistical models can subsequently be used to account for both noise and residual unmodeled effects.

4.1. Forward Scattering Model

[13] As customary in GPR problems, we split the y-directed *total* backscattered field E observed in free space at $\mathbf{r} = (x, z)$ into the background field E^b (the field in the absence of the target) and the scattered field E^s (due to the target)

$$E(\mathbf{r}, \omega) = E^b(\mathbf{r}, \omega) + E^s(\mathbf{r}, \omega), \quad (6)$$

where, via the Lippman–Schwinger equation [cf. *Chew*, 1996],

$$E^s(\mathbf{r}, \omega) = k_0^2 \int \int_{\mathcal{D}} E(\mathbf{r}', \omega) G_b(\mathbf{r}, \mathbf{r}', \omega) O(\mathbf{r}', \omega) d\mathbf{r}'. \quad (7)$$

In (7), E represents the *total* field in the target region, G_b denotes the FD Green's function of the rough-interface dielectric half-space, and

$$O(\mathbf{r}', \omega) = [\epsilon_r(\mathbf{r}') - \epsilon_{r1}] + i \frac{[\sigma(\mathbf{r}') - \sigma_1]}{\omega \epsilon_0} = \Delta\epsilon_r(\mathbf{r}') + i \frac{\Delta\sigma(\mathbf{r}')}{\omega \epsilon_0} \quad (8)$$

is the so-called object function, with $\epsilon_r(\mathbf{r}')$ and $\sigma(\mathbf{r}')$ denoting the local relative dielectric permittivity and electrical conductivity, respectively, and $\Delta\epsilon_r$, $\Delta\sigma$ defined via the last equality in (8). The integration in (7) is extended over the target region $(\mathcal{D})$ (Figure 1) wherein the object function in (8) is nonzero.

[14] The first step in our procedure consists of using the estimated surface profile to generate predictions of the background field E^b via the forward GB model of *Galdi et al.* [2002b], thereby *isolating* the scattered contribution E^s, which contains the information needed for imaging the target. Next, in view of the typically low contrast in the target scenarios of interest here (plastic antipersonnel land mines), we use the linearizing Born approximation which replaces the total field E inside the target by the transmitted field E^t in $\mathcal{D}$ in the absence of the target (see the work of *Keller* [1969] for the inherent limitations). One obtains

$$E^s(\mathbf{r}, \omega) \approx k_0^2 \int \int_{\mathcal{D}} \Delta\epsilon_r(\mathbf{r}') E^t(\mathbf{r}', \omega) G_b(\mathbf{r}, \mathbf{r}', \omega) d\mathbf{r}', \quad (9)$$

where the (weak) conductivity contrast contribution $\Delta\sigma$ in (8) has also been neglected. The inversion of the linearized model in (9) will be addressed in section 4.2. The unperturbed transmitted field E^t and the Green's function G_b in (9), which account for further distortion of the useful signal due to the twice-traversed rough air–ground interface, are computed efficiently via the PO GB syntheses detailed by *Galdi et al.* [2001b, 2002b], which are conceptually analogous to that in (5).

4.2. Object-Based Target Reconstruction: Curve Evolution

[15] The inversion of the forward scattering model in (9) is an inherently ill-posed problem, thereby implying limits of retrievable information through inverse scatter-

ing. Moreover, only limited-viewing noisy observations and approximate forward modelings are available in our problem conditions. Therefore, it is essential to incorporate stabilization via regularization methods [cf. *Bertero*, 1989; *Karl*, 2000] which, through exploiting possible a priori information, restore well-posedness by suitably restricting the solution space. In the work of *Galdi et al.* [2001b], with reference to pulsed GPRs, various *pixel-based* and *object-based* reconstruction and regularization approaches have been explored for reliable inversion of the TD counterpart of the Born-linearized forward scattering model in (9). Here, we focus on the *object-based* approaches. Unlike pixel-based approaches, where one tries to retrieve the unknown dielectric contrast $\Delta\epsilon_r$ at a number of suitably small pixels in a mosaiced test domain, object-based approaches rely on the use of parametric or semiparametric deformable shape models for the object function, which implicitly incorporate possible a priori information about the target geometry. For our specific problem, the target being homogeneous, it is suggestive to estimate the key features of the target (shape and dielectric contrast) *directly* rather than reconstruct them pointwise (with all the inherent problems of a *posteriori* edge detection). Several applications of such approaches to EM inverse scattering have been proposed in the recent past. *Chiu and Kiang* [1991a, 1991b, 1992a, 1992b] have used a shape-based formalism in conjunction with the Newton–Kantorovich technique for inverse scattering from (possibly imperfect) conducting cylinders buried in a homogeneous (possibly lossy) half-space. *Budko and van den Berg* [1998, 1999] have used an *effective* circular cylinder scattering model, with radius, permittivity and center position to be retrieved, to simulate inverse scattering due to subsurface dielectric targets. *Miller et al.* [2000] have used low-order polynomial expansions for background and target permittivity and quadratic B-spline parameterizations for the target boundary to deal with *inhomogeneous* background and targets.

[16] A particularly interesting class of object-based inversion techniques is represented by *curve evolution* (CE) [*Yezzi et al.*, 1997; *Shah*, 2000], where a *gradient flow* is designed which attracts initial closed curves to the target boundary. Such techniques, widely used in image processing, have recently been explored in EM inverse scattering problems, and have revealed attractive features from both the computational and reconstruction quality viewpoints. For instance, in the works of *Santosa* [1996], *Litman et al.* [1998], *Dorn et al.* [2000], and *Ramananjaona et al.* [2001a, 2001b], CE techniques have been applied to FD nonlinear inverse scattering problems involving penetrable targets with *known* electric properties in a homogeneous background. *Feng et al.* [2000a] and *Galdi et al.* [2001b] have explored applications to subsurface imaging of low-contrast targets in the presence of flat and moderately rough air–soil interfaces, using TD data, and we retain their approach for the latter geometry here to perform FD imaging of subsurface targets with *unknown* dielectric properties in the presence of a moderately rough air–soil interface. Although, in principle, the method can handle multiple targets, here we consider the simplest scenario with a single homogeneous target occupying the region $(\mathcal{D})$ (Figure 1) bounded by a continuous curve $\vec{C}$. To proceed, the object function in (8) is rewritten as

$$\Delta\epsilon_r(\mathbf{r}) = \overline{\Delta\epsilon_r}\Pi_{\mathcal{D}}(\mathbf{r}), \tag{10}$$

with $\overline{\Delta\epsilon_r} \equiv \epsilon_{r2} - \epsilon_{r1}$, and with $\Pi_{\mathcal{D}}$ denoting the characteristic function of the target region $\mathcal{D}$,

$$\Pi_{\mathcal{D}}(\mathbf{r}) = \begin{cases} 1, \mathbf{r} \in \mathcal{D}, \\ 0, \mathbf{r} \notin \mathcal{D}. \end{cases} \tag{11}$$

Here, prior-information-based *implicit* regularization is implemented through the homogeneity condition in (10), with the unknowns of the inverse problem now becoming the target boundary $\vec{C}$ and the single value of permittivity contrast $\overline{\Delta\epsilon_r}$.

[17] Given a set of $N_r \times N_\omega$ backscattered field observations at angular frequencies $\omega_1, \ldots, \omega_{N_\omega}$ at receiver locations $\mathbf{r}_1^r, \ldots, \mathbf{r}_{Nr}^r$(Figure 1), the problem of estimating target boundary and dielectric contrast is posed as an optimization problem involving minimization of the cost functional

$$J_{CE}\left(\vec{C}, \overline{\Delta\epsilon_r}\right) = \frac{1}{2}\sum_{p=1}^{N_r}\sum_{q=1}^{N_\omega}\left|\mathcal{E}_{pq}^s - \overline{\Delta\epsilon_r}U_{pq}\right|^2 + \beta\int_{\vec{C}} d\ell, \tag{12}$$

where $\mathcal{E}_{pq}^s \equiv \mathcal{E}^s(\mathbf{r}_p^r, \omega_q)$ represents the observed target-scattered contribution (i.e., after background field removal) at angular frequency ω_q at receiver location $\mathbf{r}_p^r$, and

$$U_{pq} = k_{0q}^2\int\int_{\mathcal{D}} E^t\left(\mathbf{r}', \omega_q\right)G_b\left(\mathbf{r}_p^r, \mathbf{r}', \omega_q\right)d\mathbf{r}', \tag{13}$$

with $k_{0q}^2 = \omega_q^2\epsilon_0\mu_0$. The first term in the cost functional in (12) enforces fidelity to the data, whereas the second term provides additional regularization by penalizing the arc length of the estimated curve, with the choice of the regularization parameter β affecting its smoothness. The proper choice of β is an important issue, and several strategies have been proposed [cf. *Hansen*, 1992]. In our implementation, β is selected empirically by trial and error, taking into account prior expectations about target geometry (e.g., convexity). Given a family of smooth curves $\vec{C}(\tau)$ parameterized by τ, the minimization of the cost functional in (12) is achieved by evolving the curve $\vec{C}(\tau)$ along the negative gradient of J_{CE} with respect to

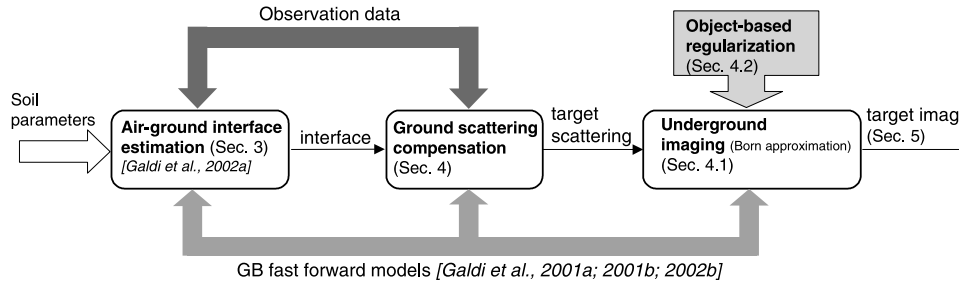

Figure 2. Schematic flowchart of the implemented adaptive approach, with appropriate references.

$\vec{C}(\tau)$ (steepest descent). Using arguments similar to those of *Feng et al.* [2000a] one finds

$$\frac{d\vec{C}(\tau)}{d\tau} = -\nabla_\tau J_{CE}\left(\tau, \overline{\Delta\epsilon_r}\right) = \sum_{p=1}^{N_r}\sum_{q=1}^{N_\omega} \cdot\left\{\left[\mathrm{Re}\left(\mathcal{E}^s_{pq}\right) - \overline{\Delta\epsilon_r}\mathrm{Re}\left[U_{pq}(\tau)\right]\right]\overline{\Delta\epsilon_r}\mathrm{Re}\left[\bar{U}_{pq}\left(\mathbf{r}'_c\right)\right] + \left[\mathrm{Im}\left(\mathcal{E}^s_{pq}\right) - \overline{\Delta\epsilon_r}\mathrm{Im}\left[U_{pq}(\tau)\right]\right] \cdot \overline{\Delta\epsilon_r}\mathrm{Im}\left[\bar{U}_{pq}\left(\mathbf{r}'_c\right)\right]\right\}\hat{\mathbf{n}}_c - \beta\kappa_c\hat{\mathbf{n}}_c, \quad (14)$$

where $\bar{U}_{pq}\left(\mathbf{r}'_c\right) = k_{0q}^2 \vec{E}^t(\mathbf{r}'_c, \omega_q) G_b(\mathbf{r}^r_p, \mathbf{r}'_c, \omega_q)$, $\mathbf{r}'_c$ denotes points on the curve $\vec{C}(\tau)$, and $\hat{\mathbf{n}}_c$ and κ_c indicate the outward normal and the signed curvature of $\vec{C}$ at $\mathbf{r}'_c$, respectively. For a given τ, the optimal value of the contrast $\overline{\Delta\epsilon_r}$ is estimated by enforcing the stationarity of (12),

$$\frac{\partial J_{CE}(\tau, \overline{\Delta\epsilon_r})}{\partial\overline{\Delta\epsilon_r}} = -\sum_{p=1}^{N_r}\sum_{q=1}^{N_\omega}\left\{\mathrm{Re}\left(\mathcal{E}^s_{pq}\right) - \overline{\Delta\epsilon_r}\mathrm{Re} \cdot\left[U_{pq}(\tau)\right]\right\}\mathrm{Re}\left[U_{pq}(\tau)\right] + \left\{\mathrm{Im}\left(\mathcal{E}^s_{pq}\right) - \overline{\Delta\epsilon_r}\mathrm{Im}\left[U_{pq}(\tau)\right]\right\}\mathrm{Im}\left[U_{pq}(\tau)\right] = 0. \quad (15)$$

For numerical convenience, the evolution in (14) needs to be discretized in τ and stepped forward. The procedure is

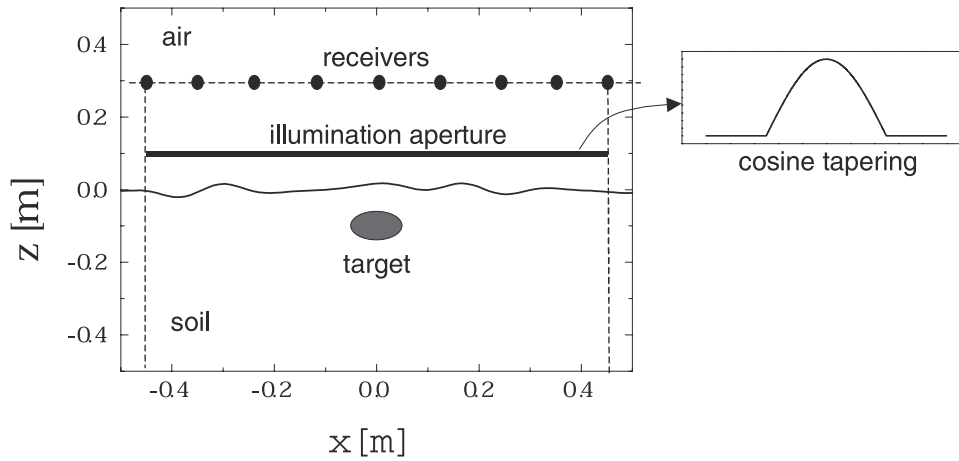

Figure 3. Simulation geometry and parameters (cf. Figure 1). Soil features: $\epsilon_{r1} = 4$, $\sigma_1 = 0.01$ S/m; roughness profile realization is generated randomly (using 20 B-spline basis functions) [*Galdi et al.*, 2002a] so as to mimic what we define as typical *moderate roughness* (maximum-to-minimum height $\sim$4 cm, maximum slope $\sim$33°). Target features: 10 × 6 cm ellipse with center at ($x = 0$, $z = -0.1$ m), $\epsilon_{r2} = 3.5$ and $\sigma_2 = 0$ buried with center at 10 cm below nominal ground (i.e., top side at 7 cm depth). Illumination: vertically incident ($\theta_A = 0$, $x_A = 0$, $z_A = 0.1$ m) cosine tapered (see (1)) with $g(x) = \cos(\pi x/d)$ ($d = 1$ m). The backscattered field is sampled at $N_r = 11$ evenly spaced receivers located at $z^r = 0.3$ m and $x^r = -0.5$ m, -0.4 m, . . ., 0.5 m.

initialized through a rough initial guess of the target boundary, which is subsequently used to obtain, via (15), the initial contrast estimate. The procedure is thus evolved, with alternative updating of the curve $\vec{C}(\tau)$ (via (14)) and of the contrast estimate $\overline{\Delta\epsilon_r}$ (via (15)) until convergence is achieved. In this connection, the target boundary initial guess was found to be not particularly critical for the overall accuracy, affecting primarily the convergence rate. Our numerical implementation is based on the level set method [*Osher and Sethian*, 1988; *Santosa*, 1996], which was found to provide numerically efficient and stable evolution. Implementation details are similar to those of *Feng et al.* [2000a] and are not discussed here.

4.3. Summary of the Proposed Approach

[18] It is useful at this point to summarize the main steps involved in our approach, in order to highlight how the various models and techniques described so far are combined to attack the *overall* problem. To this end, we refer to Figure 2, which shows a schematic flowchart of the algorithm with identification of the relevant topical references and sections in this paper. The *backbone* is provided by the GB fast forward models detailed by *Galdi et al.* [2001a, 2001b, 2002b]. The first task is the rough interface profile reconstruction from scattered field observation data, as described by *Galdi et al.* [2002a] and section 3. The resulting reconstructed interface profile is used subsequently to correct the raw observation data, compensating for ground reflection and interface (double) transmission; this yields significant clutter suppression. Target imaging is accomplished thereafter via robust inversion of the Born-linearized forward scattering model in section 4.1, using the object-based reconstruction techniques described in section 4.2.

5. Numerical Results

5.1. Simulation Parameters

[19] In order to assess the performance of the proposed subsurface imaging approach, we have carried out a broad range of numerical experiments. Here, we present and discuss typical outcomes with reference to the configuration and parameters described in Figure 3, which shows a shallowly buried plastic mine-like target in a realistic slightly lossy soil [*Hipp*, 1974] (target: 10 × 6 cm ellipse with top at 7 cm below nominal ground, $\epsilon_{r2} = 3.5$ and $\sigma_2 = 0$; soil: $\epsilon_{r1} = 4$, $\sigma_1 = 0.01$ S/m). For details, see the caption in Figure 3. Though not corresponding to any *specific* experiment, the geometric and constitutive parameters utilized here are consistent with those encountered in typical GPR applications. The Born approximation in (9) is justified in view of the relatively low permittivity contrast ($|\Delta\epsilon_r|/\epsilon_{r1} = 0.125$). This weak scattering scenario, on the other hand, renders the background field removal particularly critical.

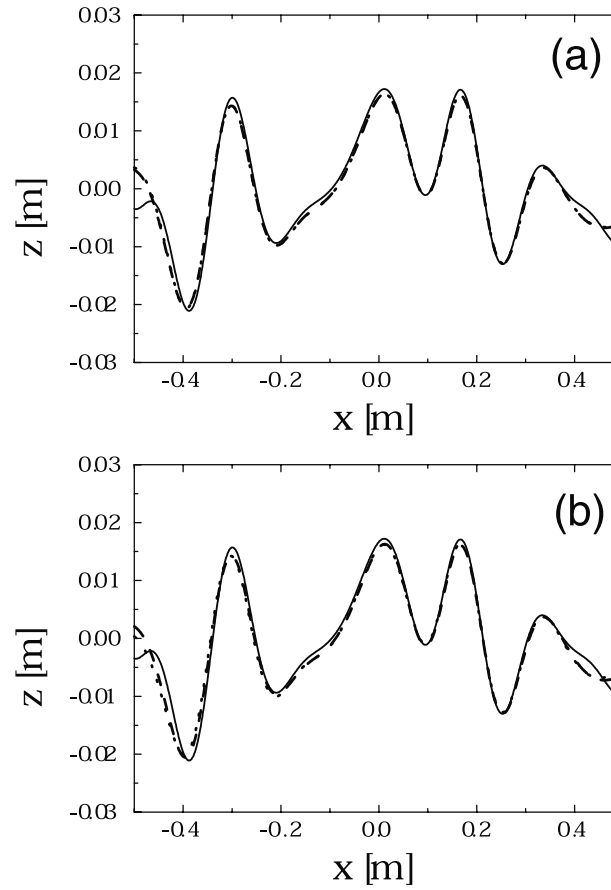

Figure 4. Parameters as in Figure 3. Rough surface profile reconstruction (cf. section 3) using a four-stage frequency-hopping scheme with $\omega_1 = 9.4 \times 10^9$ rad/s, $\omega_2 = 18.8 \times 10^9$ rad/s, $\omega_3 = 28.1 \times 10^9$ rad/s, $\omega_4 = 37.7 \times 10^9$ rad/s. A flat interface at $z = 0$ is assumed as an initial guess. Weight coefficients: $\nu_{pq} = 1$, $\forall p, q$ (see (4)). (a) Reconstructions for noiseless data and perfect knowledge of soil parameters. ---, Actual profile; —, Reconstruction (with target); ···, Reconstruction (without target). (b) Reconstructions (with target) for corrupted data or imperfect knowledge of soil parameters. —, Actual profile; ---, Reconstruction with data corrupted by additive uniform noise (±5% in magnitude, ±10° in phase); ···, Reconstruction with −5% error in ϵ_{r1} and σ_1.

[20] The backscattered field observation data $\mathcal{E}$ and $\mathcal{E}^s$ needed in (4) and (12), respectively, are simulated via a rigorous full-wave forward solver based on the multifilament current method of *Leviatan and Boag* [1987], which has been adapted here to moderately rough interfaces.

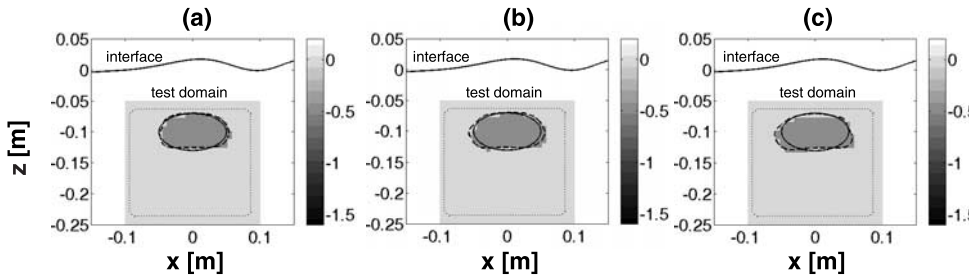

Figure 5. Examples of CE reconstructions of the relative permittivity contrast $\Delta\epsilon_r$ (dark shading) in a 20 × 20 cm test domain surrounding the target (light shading) overlaid on ground truth (solid curve reference configuration). Parameters as in Figure 3. (a) Reconstruction for noiseless observation data and perfect knowledge of air–soil interface profile and soil parameters. CE parameters (see (12)): 160 steps with $\beta = 11 \times 10^{-5}$ plus 400 steps with $\beta = 5 \times 10^{-5}$. Estimated target permittivity: $\epsilon_{r2}^{(est)} = 3.52$ (0.6% error). (b) Reconstruction for observation data corrupted by additive uniform noise (±5% in magnitude, ±10° in phase). CE parameters: 180 steps with $\beta = 14 \times 10^{-5}$ plus 1000 steps with $\beta = 3 \times 10^{-5}$. Estimated target permittivity: $\epsilon_{r2}^{(est)} = 3.58$ (2.3% error). (c) Reconstruction with −5% error in ϵ_{r1} and σ_1. CE parameters: 180 steps with $\beta = 14 \times 10^{-5}$ plus 600 steps with $\beta = 3 \times 10^{-5}$. Estimated target permittivity: $\epsilon_{r2}^{(est)} = 3.36$ (4% error). In (b) and (c), the estimated air–soil interface profiles in Figure 4b are used in the forward scattering model, and the illuminating aperture width is restricted to $d = 0.8$ m. —, Actual target boundary; --- CE-estimated target boundary; ···, CE initial conditions.

[21] Concerning the GB algorithms, a good tradeoff between accuracy and computing time was found for a beam spacing $L \sim 0.5|\lambda|$, with λ denoting the relevant ambient wavelength. This results in a computational burden about 2 times lower than the quasi-real ray-tracing scheme of *Galdi et al.* [2001a], and about 4 times lower than brute-force Kirchhoff PO implementations (with 8–10 integration points per wavelength).

5.2. Reconstruction Examples

5.2.1. Surface Estimation

[22] For the prior surface estimation problem, we have used the algorithm in section 3 in conjunction with a four-stage frequency-hopping optimization strategy at operating angular frequencies $\omega_1 = 9.4 \times 10^9$ rad/s, $\omega_2 = 18.8 \times 10^9$ rad/s, $\omega_3 = 28.1 \times 10^9$ rad/s, $\omega_4 = 37.7 \times 10^9$ rad/s. The choice of these frequencies, together with other implementation details, is discussed by *Galdi et al.* [2002a, section III-C]. Representative results are displayed in Figure 4. In order to analyze possible bias effects in the surface estimation due to the possible presence of the target, we first considered the (ideal) case of noiseless observation data and perfect knowledge of soil parameters. Figure 4a shows the reconstructions obtained *in the presence* and *in the absence* of the dielectric target. As one can see, the two reconstructions essentially coincide and, apart from the weakly illuminated edge regions, agree very well with the actual profile. In the numerical simulations we found that, for our class of low-contrast targets with $|\Delta\epsilon_r|/\epsilon_{r1} \ll 1$, the possible bias induced in the surface estimation is well below the resolution achievable with our reconstruction algorithm. In order to test the robustness of the algorithm, two examples of surface estimation for more realistic data configurations are shown in Figure 4b, namely, observation data corrupted by additive uniform noise (±5% in magnitude, ±10° in phase), and assumption of a −5% error in ϵ_{r1} and σ_1 in the forward scattering model. It is observed that the estimates are remarkably robust. In all examples above, as in the work of *Galdi et al.* [2002a], loose a priori knowledge was invoked through the initial guess of a flat interface at $z = 0$, with restriction of the surface profile search to ±8 cm around it. Moreover, the spline template used for the inversion was perfectly matched to that used for generating the roughness profile, and we focused on retrieving

Table 1. Parameters as in Figure 3, But With Different Roughness Profiles

Max. slope	Δe_t [dB]	Δe_b [dB]
33°	−28	−40
40°	−23	−38
50°	−22	−30

Target and background rms errors in (16) and (17), respectively, versus interface profile maximum slope (controlled by conformal scaling of the profile in Figure 3). The *estimated* air–soil interface profiles are used in the forward scattering model.

Table 2. As in Table 1, But Varying the Target Depth

Target depth (top side)	Δe_t [dB]	Δe_b [dB]
7 cm	−28	−40
5 cm	−27	−33
3.5 cm	−14	−27

the spline coefficients only. However, more versatile *adaptive* frameworks can be utilized [*Galdi et al.*, 2003].

5.2.2. Subsurface Imaging

[23] For the geometry and parameters in Figure 3, we next tested the CE imaging approach described in section 4.2. In all simulations presented below, we used 20 equispaced angular frequencies in the interval (6.3×10^9 rad/s, 18.8×10^9 rad/s) (i.e., in the typical GPR frequency range 1–3 GHz) which, for the assumed slightly lossy soil and shallowly buried targets, were found to provide a good tradeoff between resolution and soil penetration. The imaging is restricted to a 20 × 20 cm test domain surrounding the target which, in our CE implementation via the level set method, is discretized into 30 × 30 pixels. The observation data size was found by trial and error to provide a good tradeoff between accuracy and computational burden. The regularization parameter β in (12) was also determined pragmatically via trial and error. As stated previously, more systematic selection strategies have been proposed [e.g., *Hansen*, 1992], but this is not of prime concern here. Accordingly, the results below correspond to the best reconstructions obtained in a broad range of experiments; relative insensitivity to variation of the regularization parameter within a calibrated range (±200%) was, however, verified. Representative results are shown in Figure 5. Specifically, Figure 5a refers to the ideal case of noiseless data and perfect knowledge of soil parameters and rough interface profile. Good shape reconstruction and target permittivity estimation (0.6% error in ϵ_{r2}) are observed. Reconstructions obtained with observation data corrupted by additive uniform noise (±5% in magnitude, ±10° in phase), or by assuming imperfect knowledge of the soil parameters (−5% error in ϵ_{r1} and σ_1), are shown in Figures 5b and 5c, respectively. For these last two reconstructions, the estimated air–soil interfaces in Figure 4b were used in the forward modeling, and the illuminating aperture width was slightly reduced (d = 0.8 m) in order to de-emphasize the effect of the poorly estimated side regions in Figure 4b. Even under these more challenging conditions, reconstruction results are still quite accurate. The slightly better vertical than horizontal localization is presumably due to the limited-viewing geometry (vertical illumination), which renders the problem more ill posed in the horizontal direction.

[24] In order to better quantify the accuracy achieved in the reconstructions, we introduce two simple rms error metrics in both the target and background regions,

$$\Delta e_t \equiv 10 \log_{10} \frac{\int_{\mathcal{D}} \left[\epsilon_{r2} - \epsilon_{r2}^{(est)}(\mathbf{r}')\right]^2 d\mathbf{r}'}{\epsilon_{r2}^2 \mathcal{A}_{\mathcal{D}}}, \tag{16}$$

$$\Delta e_b \equiv 10 \log_{10} \frac{\int_{\overline{\mathcal{D}}} \left[\epsilon_{r1} - \epsilon_{r1}^{(est)}(\mathbf{r}')\right]^2 d\mathbf{r}'}{\epsilon_{r1}^2 \mathcal{A}_{\overline{\mathcal{D}}}}, \tag{17}$$

where the superscript $^{(est)}$ identifies estimated values. Moreover, $\bar{\mathcal{D}}$ is the complement (i.e., the exterior) of $\mathcal{D}$ in the test domain $\mathcal{D}^{(test)}$ of interest, whereas $\mathcal{A}_{\mathcal{D}}$ and $\mathcal{A}_{\overline{\mathcal{D}}}$ denote the areas of the domains $\mathcal{D}$ and $\overline{\mathcal{D}}$, respectively. For the examples in Figures 5a–5c, we found $\Delta e_t = -28$, −27, and −27 dB and $\Delta e_b = -42$, −38, and −25 dB, respectively (note that the considerably poorer accuracy Δe_b for the example in Figure 5c is primarily due to the assumed error in the soil permittivity).

5.3. Limitations

[25] Starting from the geometry and parameters in Figure 3, we then strained the algorithm by selecting successively more challenging simulation parameters, in order to assess its range of applicability. In particular, we selected three critical excursions: (1) roughness slope, (2) target depth, and (3) target permittivity. Results are summarized in Tables 1, 2, and 3, and are discussed below with reference to the geometry in Figure 3. The calibrated range of applicability of the algorithm, obtained through a set of 25 numerical experiments with various roughness profile realizations and soil/target parameters, is summarized in Table 4. In all simulations, the *estimated* air–soil interface profiles are used in the forward scattering model. The calibrated ranges in Table 4 were obtained by assuming as a benchmark the *best* reconstruction results achieved with our algorithm.

5.3.1. Roughness Slope

[26] Representative reconstruction results are presented concisely in Table 1, in terms of the rms errors Δe_t and Δe_b. In these experiments, the maximum slope of the roughness profile was controlled via conformal scaling of the profile in Figure 3, leaving all other parameters

Table 3. As in Table 1, But Varying the Target Permittivity

ϵ_{r2}	Δe_t [dB]	Δe_b [dB]
3.5	−28	−40
3.8	−17	−28
2.5	−7	−19

Table 4. Range of Applicability of the Implemented Approach

Parameter	Calibrated range	Specific limiting factors (if any)
Rough surface max. slope	<40°	PO approximation; imperfect interface reconstruction
Target depth (top side)	>5 cm	PO, far-field approximations; residual clutter
	<15 cm	Signal attenuation
Target contrast	$\lvert\Delta\epsilon_r\rvert/\epsilon_{r1} > 0.1$	Low visibility
	$\lvert\Delta\epsilon_r\rvert/\epsilon_{r1} < 0.25$	Born approximation
Soil losses	$\sigma_1 < 0.05\ \omega_{max}\ \epsilon_0\ \epsilon_{r1}$	Signal attenuation
Noise (uniform)	up to ±5% in magnitude, ±10° in phase	
Uncertainty in ϵ_{r1}, σ_1	up to ±5%	

Note that the "best" dB levels listed in Tables 1–3 essentially represent the best capabilities of our algorithm.

unchanged. It is observed that up to ~40°, the reconstructions are still acceptable, whereas around 50° the degradation is significant and, as shown in Figure 6a, some artifacts appear. The observed degradation is attributed primarily to the stronger residual clutter (due to imperfect reconstruction of the interface), and partially to PO-related limitations. Beyond 50°, reconstruction results were found to exhibit strong sensitivity to initial conditions and regularization parameters.

5.3.2. Target Depth

[27] Representative results are summarized in Table 2. Again, except for the target depth, the geometry and parameters are as in Figure 3. The critical minimum depth was found to be around 3.5 cm, with the corresponding reconstruction shown in Figure 6b. As one can see, in this case, apart from the very rough localization, the algorithm turns out to be unable to provide meaningful shape and contrast information. The degradation stems from the breakdown of the PO and far-field approximations utilized in our GB forward models. Another important issue is the residual clutter: even for the low-contrast target considered in these examples (resulting in practically unbiased surface reconstructions even at low target depths), for shallower targets the clutter suppression is inherently more critical. The maximum allowable depth is strongly related to the soil penetration; for the soil characteristics and operating frequencies in this example, the critical value was found to be around 15 cm.

5.3.3. Target Permittivity

[28] Representative results are summarized in Table 3, for geometry and parameters as in Figure 3. As can be expected, there exist two critical values. An exceedingly low contrast would result in a *practically invisible* target. This was found to occur for target relative permittivity around 3.8. On the other hand, an exceedingly high contrast would violate the Born approximation. In this connection, as one can see, significant deterioration in the rms errors was found for relative permittivity around 2.5. In this case, as shown in Figure 6c, the object localization is still acceptable, but the shape reconstruction contains artifacts and the contrast estimation is quite inaccurate.

5.4. Computational Aspects

[29] With specific reference to a 700 MHz PC implementation, the average computing times for the various

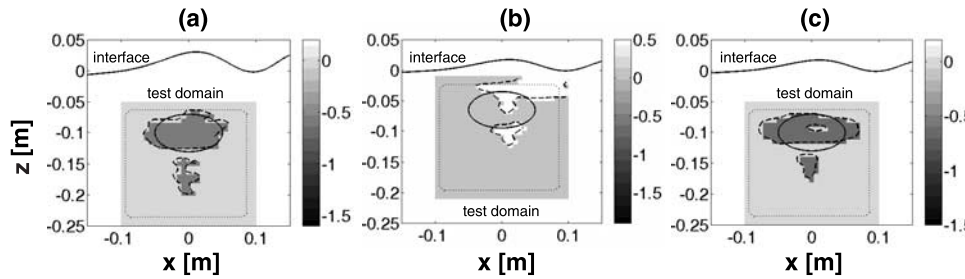

Figure 6. (a) As in Figure 5a, but with roughness profile maximum slope of 50° (estimated target permittivity: $\epsilon_{r2}^{(est)} = 3.44$, i.e., 1.7% error). (b) As in Figure 5a, but with target depth of 3.5 cm ($\epsilon_{r2}^{(est)} = 4.54$, i.e., 30% error). (c) As in Figure 5a, but with target permittivity $\epsilon_{r2} = 2.5$ ($\epsilon_{r2}^{(est)} = 3.4$, i.e., 36% error). The *estimated* air–soil interface profiles are used in the forward scattering model, and the illuminating aperture width is restricted to $d = 0.8$ m. —, Actual target boundary; ---, CE-estimated target boundary; ···, CE initial conditions.

tasks in the above approach can be summarized as follows:

1. Rough surface profile estimation: 42 s.
2. Background field removal: 0.1 s.
3. Target reconstruction: 252 s.

[30] More specifically, for the target reconstruction task via CE, the scattering functions U_{pq} in (12) are computed once and for all via the GB algorithms of *Galdi et al.* [2001b, 2002b] on a trial-and-error-selected "suitable" grid (computing time: 72 s). The curve is evolved subsequently via the level set method [*Osher and Sethian*, 1988; *Feng et al.*, 2000a] (computing time: 180 s). Memory requirements are on the order of 3 MB. Overall computing times are on the order of 5 min.

[31] We stress again that the favorable computational features of our algorithm are attributed to the GB fast forward solvers. It is interesting to note that the same conclusions were drawn by *Rao and Carin* [1999], but for a different inverse scattering scenario. For our problem, we estimate that use of more accurate full-wave solvers, though possible in principle, would require several hours of computation. For instance, a rough estimate of the overall computing time for our full-wave forward scattering reference solution [*Leviatan and Boag*, 1987] would be on the order of 4–5 hours (however, we have made no attempt to optimize the implementation).

6. Concluding Remarks

[32] The adaptive approach to 2-D GPR subsurface imaging of shallowly buried low-contrast targets (e.g., antipersonnel land mines), described in the abstract and introduction, has been documented, implemented and calibrated in this paper. Our numerical experiments have quantified the capabilities of the algorithm in terms of reconstruction accuracy and computational burden. Worthwhile extensions, currently under consideration, include performance evaluation using experimental data, and generalization of the GB forward solver to 3-D vector fields and geometries. Because the paraxial ray-like GB wave objects are localized high frequency propagators, their tractable extension to 3-D propagation and scattering environments appears promising. For some results in this connection, see the work of *Maciel and Felsen* [2001]. Alternative approaches to the surface estimation task are also under investigation. In particular, we are exploring sensor fusion strategies that involve optical range sensors, etc., which might provide more accurate surface information.

[33] **Acknowledgments.** This work was supported by ODDR&E under MURI grants ARO DAAG55-97-1-0013 and AFOSR F49620-96-1-0028 and by the Engineering Research Centers Program of the National Science Foundation under award EEC-9986821. The work of V. Galdi was also supported by a European Union postdoctoral fellowship through the University of Sannio, Benevento, Italy. L. B. Felsen also acknowledges partial support from grant 9900448 by the U.S.–Israel Binational Science Foundation, Jerusalem, Israel, and from Polytechnic University, Brooklyn, NY 11201 USA.

References

Belkebir, K., and A. G. Tijhuis, Using multiple frequency information in the iterative solution of a two-dimensional nonlinear inverse problem, in *Proc. Progress Electromagnetic Research Symp. (PIERS '96), Innsbruck, Austria*, p. 353, EMW Publ., Cambridge, Mass., 8–12 July 1996.

Bertero, M., Linear inverse and ill-posed problems, *Adv. Electron. Electron Phys.*, vol. 75, edited by P. W. Hawkes, pp. 1–120, Academic, San Diego, Calif., 1989.

Budko, N. V., and P. M. van den Berg, Two-dimensional object characterization with an effective model, *J. Electromagn. Waves Appl.*, *12*(2), 177–190, 1998.

Budko, N. V., and P. M. van den Berg, Characterization of a two-dimensional subsurface object with an effective scattering model, *IEEE Trans. Geosci. Remote Sens.*, *37*(5), 2585–2596, Sept. 1999.

Chew, W. C., *Waves and Fields in Inhomogeneous Media*, Oxford Univ. Press, New York, 1996.

Chew, W. C., and J. H. Lin, A frequency-hopping approach for microwave imaging of large inhomogeneous bodies, *IEEE Microwave Guided Wave Lett.*, *5*(12), 439–441, Dec. 1995.

Chiu, C.-C., and Y.-W. Kiang, Inverse scattering of a buried conducting cylinder, *Inverse Problems*, *7*(2), 187–202, Apr. 1991a.

Chiu, C.-C., and Y.-W. Kiang, Electromagnetic imaging for an imperfectly conducting cylinder, *IEEE Trans. Microwave Theory Tech.*, *39*(9), 1632–1639, Sept. 1991b.

Chiu, C.-C., and Y.-W. Kiang, Microwave imaging of multiple conducting cylinders, *IEEE Trans. Microwave Theory Tech.*, *40*(8), 933–941, Aug. 1992a.

Chiu, C.-C., and Y.-W. Kiang, Electromagnetic inverse scattering of a conducting cylinder buried in a lossy half-space, *IEEE Trans. Antennas Propag.*, *40*(12), 1562–1565, Dec. 1992b.

Dogaru, T., and L. Carin, Time-domain sensing of targets buried under a rough air–ground interface, *IEEE Trans. Antennas Propag.*, *46*(3), 360–372, Mar. 1998.

Dogaru, T., L. Collins, and L. Carin, Optimal time-domain detection of a deterministic target buried under a randomly rough interface, *IEEE Trans. Antennas Propag.*, *49*(3), 313–326, Mar. 2001.

Dorn, O., E. L. Miller, and C. M. Rappaport, A shape reconstruction method for electromagnetic tomography using adjoint fields and level sets, *Inverse Problems*, *16*(5), 1119–1156, Oct. 2000.

Dubey, A. C., J. F. Harvey, J. T. Broach, and V. George (eds.), *Detection and Remediation Technologies for Mines and Minelike Targets VI, Proc. SPIE*, vol. 4394, SPIE, Orlando, Fla., Oct. 2001.

Feng, H., D. A. Castañon, and W. C. Karl, Tomographic reconstruction using curve evolution, in *Proc. 2000 IEEE Conf.*

on Computer Vision and Pattern Recognition, Hilton Head Island, SC, USA, vol. 1, pp. 361–366, IEEE, Piscataway, N. J., 13–15 June 2000a.

Feng, H., D. A. Castañon, W. C. Karl, and E. L. Miller, GPR imaging approaches for buried plastic landmine detection, in *Detection and Remediation Technologies for Mines and Minelike Targets V, Proc. SPIE*, vol. 4038, edited by A. C. Dubey et al., pp. 1485–1496, SPIE, Orlando, Fla., Aug. 2000b.

Galdi, V., L. B. Felsen, and D. A. Castañon, Quasi-ray Gaussian beam algorithm for time-harmonic two-dimensional scattering by moderately rough interfaces, *IEEE Trans. Antennas Propag.*, *49*(9), 1305–1314, Sept. 2001a.

Galdi, V., L. B. Felsen, and D. A. Castañon, Gaussian beam algorithms for rough surface underground imaging, in *Proc. 7thInt. Conference on Electromagnetics in Advanced Applications (ICEAA '01), Torino, Italy*, pp. 175–178, Polytech. Univ. of Turin, Turin, Italy, 10–14 Sept. 2001b.

Galdi, V., D. A. Castañon, and L. B. Felsen, Multifrequency reconstruction of moderately rough interfaces via quasi-ray Gaussian beams, *IEEE Trans. Geosci. Remote Sens.*, *40*(2), 453–460, Feb. 2002a.

Galdi, V., L. B. Felsen, and D. A. Castañon, Quasi-ray Gaussian beam algorithm for short-pulse two-dimensional scattering by moderately rough dielectric interfaces, *IEEE Trans. Antennas Propag.*, *50*(12), in press, Dec. 2002b.

Galdi, V., J. Pavlovich, W. C. Karl, D. A. Castañon, and L. B. Felsen, Moderately rough dielectric interface reconstruction via short-pulse quasi-ray Gaussian beams, *IEEE Trans. Antennas Propag.*, *51*(3), in press, Mar. 2003.

Hansen, P. C., Analysis of discrete ill-posed problems by means of the L-curve, *SIAM Rev.*, *34*(4), 561–580, Dec. 1992.

Hipp, J. E., Soil electromagnetic parameters as functions of frequency, soil density, and soil moisture, *Proc. IEEE*, *62*(1), 98–103, Jan. 1974.

Karl, W. C., Regularization in image restoration and reconstruction, in *Handbook of Image and Video Processing*, edited by A. Bovik, pp. 141–160, Academic, San Diego, Calif., 2000.

Keller, J. B., Accuracy and validity of the Born and Rytov approximations, *J. Opt. Soc. Am.*, *59*(8), 1003–1004, Aug. 1969.

Leviatan, Y., and A. Boag, Analysis of electromagnetic scattering from dielectric cylinders using a multifilament current model, *IEEE Trans. Antennas Propag.*, *35*(10), 1119–1127, 1987.

Litman, A., D. Lesselier, and F. Santosa, Reconstruction of a two-dimensional binary obstacle by controlled evolution of a level set, *Inverse Problems*, *14*(3), 685–706, June 1998.

Maciel, J. J., and L. B. Felsen, Gabor-based narrow-waisted Gaussian beam algorithm for transmission through a spherically layered radome, in *Proc. 2001 IEEE Antennas and Propagat. Int. Symp., Boston, MA,* vol. 1, pp. 570–573, IEEE, Piscataway, N.J., 8–13 July 2001.

Miller, E. L., M. Kilmer, and C. Rappaport, A new shape-based method for object localization and characterization from scattered field data, *IEEE Trans. Geosci. Remote Sens.*, *38*(4), 1682–1696, July 2000.

Osher, S., and J. Sethian, Fronts propagation with curvature dependent speed: Algorithms based on Hamilton–Jacobi formulations, *J. Comp. Phys.*, *79*(1), 12–49, Nov. 1988.

Ramananjaona, C., M. Lambert, D. Lesselier, and J.-P. Zolésio, Shape reconstruction of buried obstacles by controlled evolution of a level set: From a min–max formulation to numerical experimentation, *Inverse Problems*, *17*(4), 1087–1111, Aug. 2001a.

Ramananjaona, C., M. Lambert, and D. Lesselier, Shape inversion from TM and TE real data by controlled evolution of level sets, *Inverse Problems*, *17*(6), 1585–1595, Dec. 2001b.

Rao, B., and L. Carin, Beam-tracing-based inverse scattering for general aperture antennas, *J. Opt. Soc. Am. A Opt. Image Sci.*, *16*(9), 2219–2231, Sept. 1999.

Santosa, F., A level-set approach for inverse problems involving obstacles, *ESAIM, Control Optim. Calc. Var.*, *1*, 17–33, 1996.

Shah, J., Riemannian drums, anisotropic curve evolution, and segmentation, *J. Vis. Commun. Image Represent.*, *11*(2), 142–153, June 2000.

Shumaker, L. L., *Spline Functions: Basic Theory*, John Wiley, New York, 1981.

Yang, B., and C. M. Rappaport, Response of realistic soil for GPR applications with 2-D FDTD, *IEEE Trans. Geosci. Remote Sens.*, *39*(6), 1198–1205, June 2001.

Yezzi, A., S. Kichenassamy, K. Kumar, P. Olver, and A. Tennenbaum, A geometric snake model for segmentation of medical imagery, *IEEE Trans. Med. Imag.*, *16*(2), 199–209, 1997.

Zhan, H., C. M. Rappaport, M. El-Shenawee, and E. L. Miller, Mine detection under rough ground surfaces using 2-D FDTD modeling and hypothesis testing, in *Proc. 2001 IEEE Antennas Propagat. Int. Symposium, Boston, MA, USA*, vol. 3, p. 756, IEEE, Piscataway, N.J., 8–13 July 2001.

D. A. Castañon, H. Feng, and W. C. Karl, Department of Electrical and Computer Engineering, Boston University, 8 Saint Mary's Street, Boston, MA 02215, USA. (dac@bu.edu; hfeng@bu.edu; wckarl@bu.edu)

L. B. Felsen, Department of Aerospace and Mechanical Engineering, Boston University, 110 Cummington Street, Boston, MA 02215, USA. (lfelsen@bu.edu)

V. Galdi, Dipartimento di Ingegneria, Universita del Sannio, Pallazo Dell'Aquila Bosco Lucarelli, Corso Garibaldi 107, I-82100 Benevento, Italy. (vgaldi@unisannio.it)